Journal of Comparative Physiology A (2021) 207:757–772
https://doi.org/10.1007/s00359-021-01518-x

ORIGINAL PAPER

Inflight head stabilization associated with wingbeat cycle and sonar emissions in the lingual echolocating Egyptian fruit bat, *Rousettus aegyptiacus*

Jackson Rossborough[1] · Angeles Salles[3] · Laura Stidsholt[4] · Peter T. Madsen[4] · Cynthia F. Moss[3] · Larry F. Hoffman[1,2]

Received: 14 July 2021 / Revised: 12 October 2021 / Accepted: 14 October 2021 / Published online: 30 October 2021

Abstract

Sensory processing of environmental stimuli is challenged by head movements that perturb sensorimotor coordinate frames directing behaviors. In the case of visually guided behaviors, visual gaze stabilization results from the integrated activity of the vestibuloocular reflex and motor efference copy originating within circuits driving locomotor behavior. In the present investigation, it was hypothesized that head stabilization is broadly implemented in echolocating bats during sustained flight, and is temporally associated with emitted sonar signals which would optimize acoustic gaze. Predictions from these hypotheses were evaluated by measuring head and body kinematics with motion sensors attached to the head and body of free-flying Egyptian fruit bats. These devices were integrated with ultrasonic microphones to record sonar emissions and elucidate the temporal association with periods of head stabilization. Head accelerations in the Earth-vertical axis were asymmetric with respect to wing downstroke and upstroke relative to body accelerations. This indicated that inflight head and body accelerations were uncoupled, outcomes consistent with the mechanisms that limit vertical head acceleration during wing downstroke. Furthermore, sonar emissions during stable flight occurred most often during wing downstroke and head stabilization, supporting the conclusion that head stabilization behavior optimized sonar gaze and environmental interrogation via echolocation.

Keywords Gaze stabilization · Acceleration · Tongue clicks · Motion tag · Echolocation

Introduction

Successful animal navigation requires sensory monitoring of targets and obstacles in the environment, which can be compromised by head and body movements associated with locomotion. The sensorimotor mechanisms implemented during natural behaviors typically reference head-centric coordinate frames to achieve *sensory gaze* stabilization. The vestibulo-ocular reflex (VOR) is an important component of visual gaze stabilization, whereby inner ear vestibular receptors encode head kinematics leading to compensatory eye movements that stabilize visual targets on the retina (du Lac et al. 1995; Straka and Dieringer 2004). Mechanisms of head stabilization contribute to visual gaze stabilization during ambulatory activity, thereby optimizing performance of the VOR (Shanidze et al. 2010; Goldberg and Cullen 2011; Dietrich and Wuehr 2019a; Dietrich et al. 2020). In birds, head movements are the predominant means of visual gaze stabilization (Land 2015). These movements can be particularly well refined as demonstrated in a study showing that ultrafast head saccades were invoked for visual gaze stabilization during rapid inflight direction reversal (i.e., "turn-on-a-dime") maneuvers executed by lovebirds (Kress et al. 2015). The head saccades were initiated most often during

Jackson Rossborough, Angeles Salles and Laura Stidsholt contributed equally to the research and manuscript.

✉ Larry F. Hoffman
lfh@g.ucla.edu

[1] Department of Head and Neck Surgery, David Geffen School of Medicine at UCLA, Box 951624, Los Angeles, CA 90095-1624, USA

[2] Brain Research Institute, David Geffen School of Medicine at UCLA, Los Angeles, CA 90095, USA

[3] Department of Psychological and Brain Sciences, Johns Hopkins University, Baltimore, MD 21218, USA

[4] Department of Biology, Aarhus University, Aarhus, Denmark

the start of the wing downstroke. The authors interpreted these findings to reflect the superposition of behaviors that impair vision (i.e., visual blurring during head movements, and occlusion of the lateral visual field by the wing downstroke), leaving the balance of the total wingbeat cycle with uncompromised vision (Kress et al. 2015). This behavior exemplifies active head movements supporting sensory gaze stabilization with a tendency to be temporally associated with a particular phase of the wingbeat cycle.

Comparable gaze stabilization mechanisms for other head-centric sensory modalities have also been investigated. Of particular interest are mechanisms of acoustic gaze stabilization in bats that utilize biological sonar to probe their environment during flight to avoid obstacles, localize conspecifics, and intercept prey (Ghose and Moss 2006; Surlykke et al. 2009; Chiu et al. 2010). Direction control of the sonar beam is an example of an important effector component of acoustic gaze stabilization utilized by bats employing laryngeal echolocation (Ghose and Moss 2003), as well as lingual echolocation, such as Egyptian fruit bats [*Rousettus aegyptiacus* (Yovel et al. 2010, 2011; Lee et al. 2017)]. Absent from these previous investigations, however, were measurements of head kinematics and their role in acoustic gaze stabilization.

Eitan et al. (2019) recently investigated acoustic gaze stabilization, using videographic analyses to measure inflight head and body movements. They found that head movements were strongly attenuated compared to the body center of mass during short flight segments in a target identification and landing task. This result revealed the uncoupling of head movements from oscillatory body movements associated with wingbeats, and suggested the implementation of specific mechanisms for head stabilization (Eitan et al. 2019). The authors provided evidence that head stabilization was highly refined as the bats approached a landing target, even while body movements were quite large. These findings suggest that echolocating bats may exhibit even more refined mechanisms than birds for inflight head stabilization during landing. However, the relation between head and body movements during sustained flight has yet to be investigated.

Furthermore, Eitan et al. (2019) argued that bat head stabilization strongly depended upon mechanisms associated with echolocation-mediated target acquisition, and was not strictly driven by vestibular-mediated compensatory reflexes. However, the timing of sonar clicks with respect to head kinematics, fundamental to acoustic gaze stabilization, was not measured in their study. The present investigation bridges this gap by directly measuring the temporal relationship between sonar click production and head kinematics in flying Egyptian fruit bats.

The present investigation was undertaken to achieve two principal objectives. First, onboard motion sensors were used to measure head and body kinematics during sustained flight, extending the observations of Eitan et al. (2019) to an additional flight repertoire of the Egyptian fruit bat. Second, the link between sonar emissions and head kinematics was established for this lingual echolocating species. It was hypothesized that Egyptian fruit bats control the timing of sonar clicks to optimize acoustic gaze stabilization. The specific prediction emerging from this hypothesis is that sonar clicks are temporally associated with the particular phase of the wingbeat cycle when head movements exhibit the greatest attenuation relative to body movements, revealing maximal head stabilization.

Methods

Animals

The data reported herein were collected from two Egyptian fruit bats (*R. aegyptiacus*), selected randomly from a small colony of healthy adult animals. The female and male subjects were referred to as *Blue* and *Red,* and had body masses of 163 and 218 g, respectively. All experimental procedures involving animals were conducted at Johns Hopkins University and conformed to the protocol approved by the JHU institutional animal care and use committee. During the course of their training for this and another experiment, analyses of a short flight task were made to evaluate their general flight characteristics. *Blue* and *Red* were trained to land on a target, and video records were obtained under infrared light as they flew across an empty flight room (without the motion tags used to monitor head and body kinematics; see below). Flight velocities and wingbeat frequencies were evaluated by offline tracking the subjects' body and wing motion using DLTdv Hedrick Lab *Matlab* toolbox (Hedrick 2008). Four and five trials for *Blue* and *Red*, respectively, were analyzed (one trial for *Blue* was discarded due to artifacts in the recording). Mean flight velocities (± standard deviation) for *Blue* and *Red* were found to be 1.93 ± 0.66 m s^{-2} and 1.71 ± 0.36 m s^{-2} (respectively), and wingbeat frequencies were 8.4 ± 1.73 Hz and 9.6 ± 1.6 Hz (respectively). These data from randomly selected subjects illustrate the similarity in their flight characteristics despite differences in body mass.

Inflight head and body movements, as well as the animals' sonar emissions, were recorded as they flew across a flight room (6 m × 6 m × 2.5 m) under infrared illumination. They were trained to locate and land on a roosting perch. Upon successful landing they were rewarded with banana and allowed to rest 1 minute before being retrieved and repeating the task. The animals were not food deprived during training, and as such this training required more than 1 month. Sessions lasted no longer than 30 min and the animals were monitored for any sign of discomfort or abnormality in their

flying. During training, bats flew perpendicular to the walls of the flight room. During testing with the motion tags (see below), bats were prompted to fly diagonally in the room to maximize each stable flight epoch. The trajectories to the landing platform were not uniform across trials.

Inflight kinematics and audio recording

Head and body kinematics during flight segments were recorded by *motion tags* (Fig. 1a) placed on the skull and interscapular region of the back, between the wings (Fig. 1b). The tags were attached with water-soluble theater glue [Hydro Mastix; Kryolan (Warnecke et al. 2018)] to the animal's fur and removed after each session. The animals were not anesthetized during this procedure, but were hand-restrained by one investigator while another attached the tags. The size of the bat's head and targeted interscapular region on the back enabled consistent placement throughout the data collection trials. The motion tags, previously described in detail (Stidsholt et al. 2019), included a triaxial accelerometer, triaxial magnetometer (Kionix KX022) and an ultrasonic microphone (Knowles, FG-23329). They also included a 45mAh lithium-ion battery, on-board signal processing, and 8 GB flash memory for data storage (Stidsholt et al. 2019). Each tag had a mass of 2.6 g, and collectively (5.2 g total load for both tags) represented 3.2% and 2.4% of the body masses for *Blue* and *Red*, respectively. These additional loads may require as much as 5% additional power to sustain flight, but would likely have minimal impact (i.e., < 2.5%) on maneuverability (< 2.5%; see Aldridge and Brigham 1988). These devices were used in a previous study of body kinematics and direction heading in the European (common) noctule (*Nyctalus noctula*; 26–30 g) and the big brown bat (*Eptesicus fuscus*; 14–18 g), for which no anomalous effects of carrying the back-mounted tags on flight performance were noted for short-term deployments (Stidsholt et al. 2019).

The triaxial accelerometers incorporated into the motion tags measured linear acceleration along the *x*, *y*, and *z* axes depicted by the orientation compass shown in Fig. 1a. These

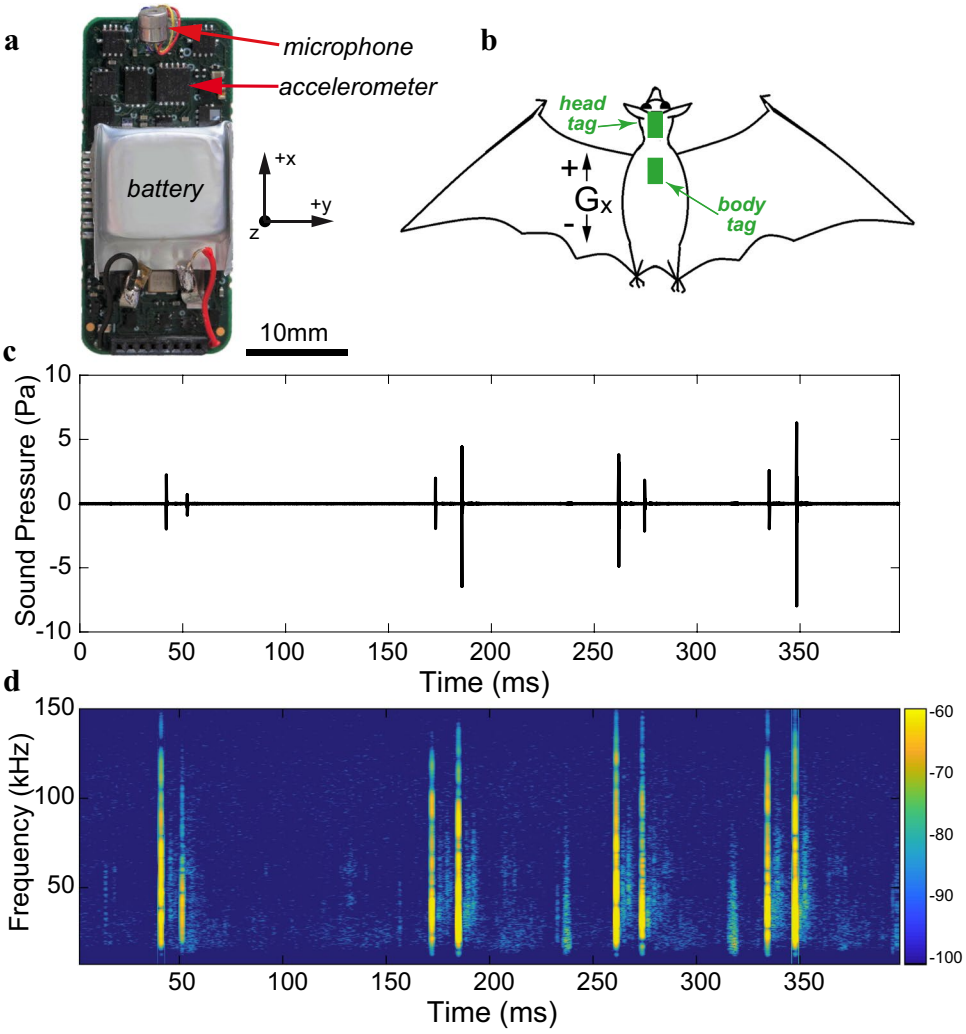

Fig. 1 Motion tag packages placed on head and back of two *R. aegyptiacus* subjects for recording inflight kinematics and sonar emissions. **a** The motion tag package was a single-board device that included a triaxial accelerometer and ultrasonic microphone. The battery is also identified. Orientations of the three acceleration vectors are shown by the compass (+ G_z projects out of the page toward reader). **b** Diagram of *R. aegyptiacus* showing approximate placement of head and body tags. The direction of G_x is shown to confirm orientation of the tags relative to body axes. **c** The filtered output of the ultrasonic microphone clearly shows the doublet pattern of tongue clicks emitted by *R. aegyptiacus*. The spectrogram of this emitted recorded segment is shown in (**d**), illustrating that the doublets are composed of audio frequencies exceeding 100 kHz. Spectrogram intensity scale in units of dB/kHz

measures are indicated by G_x, G_y, and G_z throughout the manuscript. Axis-specific acceleration measures from the motion tag attached to the head are represented as $G_{x\mathrm{H}}$, $G_{y\mathrm{H}}$, and $G_{z\mathrm{H}}$, while measures from the body motion tag are represented as $G_{x\mathrm{B}}$, $G_{y\mathrm{B}}$, and $G_{z\mathrm{B}}$. The motion tags were oriented on each animal to qualitatively align the G_x axis with the long axes of the animals' bodies (Fig. 1a, b; see compass). The accelerometers featured 16-bit sampling at 1k samples/s for each channel, and onboard processing included a 250 Hz 4-pole anti-aliasing filter. These data were downsampled offline to produce accelerometer measures at 100 samples/s.

Sonar tongue clicks emitted during flight were recorded by the ultrasonic microphone sampled at 187.5 kHz (Fig. 1a, c, d). Onboard processing of microphone recordings included a first stage 80 kHz 4-pole anti-aliasing filter, followed by a second filtering stage (i.e., 10 kHz, 1-pole high-pass filter) to reduce wind and wing noise. This processing strategy was sufficient for recording the broadband clicks emitted by *R. aegyptiacus* that typically exhibit peak energy at approximately 35 kHz (Lee et al. 2017). This preprocessed audio channel was then digitized at 16-bits and stored in flash memory. Further offline processing (described below) was implemented to unambiguously identify the ultrasonic tongue clicks emitted by the *R. aegyptiacus* subjects (Fig. 1c, d).

Analyses of inflight head and body kinematics

Synchronizing head and body tags

To compare the acceleration data collected by head and body motion tags, it was necessary to temporally synchronize the recordings. This was achieved by presenting an external audio signal that could be recovered in the respective audio channels of each tag. The audio records from both motion tags were aligned on this recorded signal. The onboard microcontroller software implemented a 50 ms delay in recording data from the accelerometer, necessitating a corresponding time shift in the accelerometer data channels, but were otherwise temporally synchronized and sampled by the same onboard clock.

Selection and analysis of stable flight periods

An example of inflight body kinematic behavior of one *R. aegyptiacus* subject (*Red*) is shown in Fig. 2, illustrating for one subject the episodic periods of flight that was exhibited by both animals in the flight room. Among all flight episodes, those selected for analysis exhibited a minimum duration of 1.6 s. The first and last 2–3 wingbeat cycles of each flight were omitted to avoid take-offs and landings, thereby identifying periods of sustained flight in the middle of each episode. The *Matlab* function *findpeaks()* was used to identify the peaks and troughs of head and body G_z for each flight epoch that conformed to specific criteria for minimum inter-peak/trough period (7 samples, or 0.07 s) and minimum magnitude ($0.5g$). Troughs were identified by inverting the acceleration epoch polarity and applying the *findpeaks()* function, in these cases utilizing a minimum magnitude of $0.2g$. A total of 25 flight epochs were analyzed from each subject, producing a total of 464 and 522 wingbeat cycles for *Blue* (47.1% of the total) and *Red* (52.9% of the total) subjects, respectively. These flight epochs were utilized for all analyses, including those of the temporal correlation of tongue click onset and G_z.

Accelerometer data

All accelerometer data used in the present analyses were calibrated by aligning the z axes of each motion tag parallel with Earth gravity, representing 9.8 m s^{-2}, and then converting to g ($1g = 9.8$ m s^{-2}) to produce axial acceleration of G_z for head and body tags (i.e., $G_{z\mathrm{H}}$ and $G_{z\mathrm{B}}$). Acceleration data reflect the direct measures from each tag.

Estimation of $G_{z\mathrm{H}}$ gain

Stabilization of the head during locomotion reflects attenuation of head kinematics relative to body kinematics, the latter representing the "forcing function" to be attenuated for multisystem sensory gaze stabilization (Pete et al. 2015). The initial approach adopted to analyze head kinematics relative to body movements was initially based upon simply computing the magnitude difference between $G_{z\mathrm{H}}$ and $G_{z\mathrm{B}}$ at maximum wing downstroke and upstroke magnitudes. Though substantial evidence is presented to the contrary, the interpretation of such G_z magnitude differences could be ambiguous due to the potential superposition of static head tilt and wingbeat oscillation (Fig. 4). Analyses of the three acceleration axes to produce a single Euclidean acceleration vector and reveal the contribution of head tilt to the modulation of $G_{z\mathrm{H}}$ (i.e., through the effect of Earth gravity on $G_{x\mathrm{H}}$) was not possible due to the integration of flight acceleration along the $G_{x\mathrm{H}}$ axis. To further confirm the independence $G_{z\mathrm{H}}$ asymmetry from the influence of static tilt, $G_{z\mathrm{H}}$ *gain* at peak downstroke and upstroke (i.e., for each inflight half-cycle). The magnitudes of peak and trough $G_{z\mathrm{H}}$ and $G_{z\mathrm{B}}$ for each wingbeat were computed as the difference between the maximum magnitude and the respective mean $G_{z\mathrm{H}}$ or $G_{z\mathrm{B}}$ for each respective flight epoch. $G_{z\mathrm{H}}$ gains (re: $G_{z\mathrm{B}}$, in dB) for each inflight half-cycle were computed from the following equation:

$$\mathrm{Gain} = 20 \cdot \log(G_{z\mathrm{H}} \cdot G_{z\mathrm{B}}^{-1}).$$

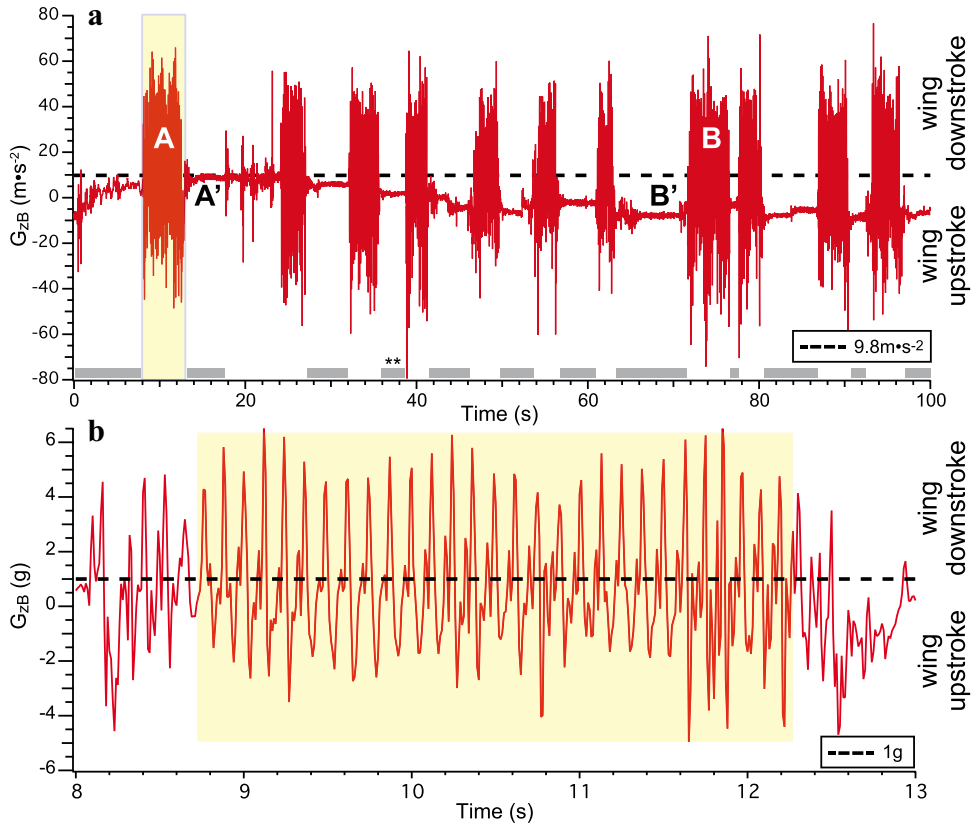

Fig. 2 Laboratory flights comprised of short epochs. **a** Episodic flights of one *R. aegyptiacus* subject (Red) within the JHU flight room represented by modulation of G_{zB}. Wing downstrokes resulted in an upward (antigravity) force that were greater than Earth gravity (9.8 m s^{-2}; dashed horizontal line), while wing upstrokes generated force vectors in the opposite direction. The flight periods labeled *A* and *B* highlight epochs immediately before and after periods marked *A'* and *B'*, respectively, representing rest periods exhibiting markedly different G_{zB} measures ($+8.9 \pm 0.69$ m s^{-2} and -7.8 ± 0.64 m s^{-2}, respectively). Flight epochs *A* and *B* were further analyzed to demonstrate the absence of sensor drift (see Supplemental Figure 1). The gray bars immediately above the abscissa denote the periods of rest between flight epochs (double asterisk denotes period where $G_{zB} = 0$ m s^{-2}). The first epoch (yellow highlight) is shown at higher temporal resolution in (**b**). **b** Expanded temporal view of G_{zB} highlighted flight epoch from (**a**). Within this epoch, a subsegment was selected for detailed analysis representing stable flight, avoiding short periods after takeoff and before landing. Acceleration magnitudes were converted to *g* (9.8 m s^{-2}/g). Maximum downstroke acceleration magnitudes (*peaks*) range from approximately 4 to 6*g*, while maximum upstroke acceleration magnitudes (*troughs*) range −2 to −4*g*

Analyses of inflight audio

Identification of tongue clicks

Audio recordings during the flight epochs selected for head and body kinematic analyses were analyzed for sonar emissions. A 4-pole high-pass Butterworth filter (15 kHz corner frequency) was used to remove low frequency components not associated with *R. aegyptiacus* tongue clicks (Griffin et al. 1958). It was implemented in *Matlab* using the *filtfilt()* function, a digital filter function that did not induce phase shifts or temporal delays in the resulting audio signal. Echolocation clicks emitted by the bats could then be readily identified as high frequency transients in the recorded audio channel (Fig. 1c, d). The *Matlab* function *findpeaks()* was used to locate these transients in the audio recordings with interpeak times that ranged 16–28 ms and exceeded a minimum amplitude threshold of 0.75 Pa.

Head kinematics at click onset

Previous studies have suggested that inflight head stabilization behaviors in birds are executed to optimize visually guided flight (Kress et al. 2015; Land 2015). A comparable behavioral paradigm in echolocating bats would be supported by the association of head stabilization with the onset of sonar emissions to optimize acoustic gaze. To evaluate this association, we determined G_{zH} and G_{zB} magnitude at the onset of sonar emissions, represented by the first emission of the tongue click doublet. Since the sampling frequency of the acoustic recording was orders of magnitude greater than that of the acceleration channels, G_{zH} and G_{zB} magnitudes at first click times

were determined by linear interpolation. This was achieved by estimating the acceleration magnitude at the precise click onset time using the *Matlab* function *interp1()* from measured acceleration values immediately before and after these emission times.

Statistical analyses

The statistical analyses in the present investigation consisted primarily of comparisons of measurement distributions shown as box-and-whisker plots representing medians, 25th and 75th percentiles (box), and the 2nd and 98th percentiles (whiskers).

Similar to the strategy utilized by Eitan et al. (2019) in their evaluation of the angles between flight direction (determined from body position) and target, and between head position and target, head stabilization behaviors were interpreted to be represented by the uncoupling of head and body accelerations along the *z*-axis (i.e., G_z) during portions of each wingbeat cycle. The present dataset utilized the distributions of head and body acceleration measures provided by the motion tags, from which temporally associated maxima in positive and negative values (i.e., acceleration peaks and troughs) were identified. Differences in $G_{z\mathrm{H}}$ and $G_{z\mathrm{B}}$ measures at the peaks and troughs were determined and produced new distributions providing an index to the uncoupling, from which changes in head and body kinematics were inferred. These distributions were compared by computing the Kullback–Leibler divergence (D_{KL}; Mackay 2003), representing a measure of the relative entropy between the two distributions. We then implemented bootstrap resampling to produce a distribution of 10^6 D_{KL} values computed from random association of peak and trough $G_{z\mathrm{H}}$ and $G_{z\mathrm{B}}$ measures. This provided the basis for determining the explicit probability that the empirical D_{KL} value could have resulted randomly.

The general strategy described above was executed through evaluations of null hypotheses that the distributions subject to comparison were similar, which were achieved by determining the probability that the empirical D_{KL} (i.e., computed from the empirical distributions) could have resulted from random bootstrap sampling from the pertinent distributions of acceleration measures. That is, D_{KL} values were computed from one million randomly resampled distributions to generate null distributions of D_{KL} measures. The probabilities that the empirical D_{KL} value could have been achieved from random resampling of acceleration measures were then determined and reported.

Results

Inflight G_z and identification of sustained flight

The brief, episodic flights typical for bats in a laboratory flight room are shown in Fig. 2a (e.g., Stidsholt et al. 2019). These data represent the calibrated recording of G_z from the body motion tag ($G_{z\mathrm{B}}$ accelerometer axis orthogonal to the tag's long axis; Fig. 1a). For the *R. aegyptiacus* subjects of the present study individual epochs ranged 1.6–4 s in duration. These oscillations are the result of wing downstrokes generating accelerations against Earth gravity (> 9.8 m s^{-2}), and upstrokes generating accelerations coincident with Earth gravity (< 9.8 m s^{-2}). Hence, the oscillations in $G_{z\mathrm{B}}$ were a direct reflection of wingbeats, interspersed with brief periods in which the animal lands and rests (also depicted as the gray bars along the horizontal axis), often with the body in a nonorthogonal position relative to Earth gravity resulting in $G_{z\mathrm{B}}$ measures $< 1g$. For example, when the *z* accelerometer axis is orthogonal to Earth gravity $G_{z\mathrm{B}} = 0$ m s^{-2} (e.g., double-asterisk-marked gray bar in Fig. 2a at approximately 36–38 s).

Figure 2a demonstrates that measures of $G_{z\mathrm{B}}$ during interflight rest periods exhibited acceleration levels that ranged between approximately 9.8 and -9.8 m s^{-2}, which likely represented the heterogeneity in body positions when the animal landed. An alternative explanation was that it reflected sensor drift instability in the static measures of G_z (e.g., *A*' and *B*'). To examine this possibility, $G_{z\mathrm{B}}$ oscillations during flight epochs immediately before and after rest periods during which static $G_{z\mathrm{B}}$ measures were approximately 9.8 m s^{-2} and -9.8 m s^{-2} (i.e., Fig. 2a, marked as *A* and *B*, respectively) were compared (Supplemental Figure 1). If sensor drift were the basis for differences in $G_{z\mathrm{B}}$ during the interflight rest periods, it was expected that this would also result in a static offset in $G_{z\mathrm{B}}$ during the flight measurements and would appear as a decrease in the median $G_{z\mathrm{B}}$ of period *B*. This negative offset condition is exemplified by the distribution modeled as b_{offset}, implemented by uniformly applying an offset of -9.8 m s^{-2} to each value of the distribution in period *b*. Comparison of $G_{z\mathrm{B}}$ during flight periods *A* and *B* demonstrated that they were similar, inferring that the rest period offset was independent of $G_{z\mathrm{B}}$ measures during flight. However, comparison of $G_{z\mathrm{B}}$ during period *a* and b_{offset} inferred that an offset of only -9.8 m s^{-2} resulted in a distribution dissimilar to the distributions in $G_{z\mathrm{B}}$ during flight ($p = 0.0012$). These analyses support the conclusion that $G_{z\mathrm{B}}$ heterogeneity during the interflight rest periods were not the result of sensor drift and measurement offset.

Figure 2b shows the highlighted flight segment from Fig. 2a (yellow) after expanding the time axis to illustrate $G_{z\mathrm{B}}$ accelerations with each wingbeat. Most wingbeats show greater peak $G_{z\mathrm{B}}$ acceleration during wing downstroke than upstroke, consistent with previous descriptions of the heterogeneous forces corresponding with each wingbeat half-cycle (Aldridge 1987; Hedenstrom and Johansson 2015). The shaded region exemplifies the *sustained* portion of the flight epoch selected for analysis of head and body kinematics that

excluded the onset and termination portions exhibiting more unstable accelerations associated with takeoff and landing. The analyzed flight epoch shown in Fig. 2b was approximately 3.4 s and included 28 wingbeat cycles. The mean period for these wingbeats was 0.121 s, corresponding to a mean frequency of 8.3 Hz. The median wingbeat period for each subject over all analyzed flight epochs was 0.12 s, similar to previously reported measurements for *R. aegyptiacus* (Yartsev and Ulanovsky 2013).

Heterogeneity in the peaks and troughs of G_{zH} and G_{zB} suggests kinematic uncoupling

The record of G_{zB} in Fig. 2a illustrates that measurements of acceleration reflect both dynamic (i.e., due to wingbeats) and static (i.e., due to changes in orientation affecting Earth gravity sensing) forces to produce composite measurements of head and body acceleration along the G_z axis. We evaluated G_{zH} in the context of G_{zB} for evidence that the head was either coupled or uncoupled from the body. Evidence that the head and body were consistently uncoupled over the 986 wingbeat cycles in both subjects would strongly infer the implementation of specific behaviors to stabilize the head during flight.

The data in Fig. 3a, b demonstrate a consistent asymmetry in the peaks and troughs of G_{zH} relative to G_{zB} highlighted by the symbols marking these local (i.e., wingbeat cycle-by-cycle) positive and negative maxima in G_z. That is, the differences between peak G_{zH} and G_{zB} appear to be greater than the differences between the troughs of G_{zH} and G_{zB}. These differences are illustrated by box-and-whisker plots in Fig. 3c, d, representing the distributions of all G_{zH} and G_{zB} measures at the acceleration peaks and troughs for *Blue* and *Red* subjects (respectively). These analyses confirm that the relationships demonstrated in the 2-s flight raw data (Fig. 3a, b) were consistently observed over the 986 wingbeat cycles of both subjects. In view of the similarities across each subject, these data were combined in Fig. 3e showing box-and-whisker plots of the differences between G_{zH} and G_{zB} at the maxima and minima. These values were computed as the differences in absolute values between G_{zH} and G_{zB} for both trough and peak accelerations in each wingbeat cycle. The data show that the differences in G_{zH} and G_{zB} for peak maxima appear to be larger than the differences in trough G_{zH} and G_{zB}.

The peak and trough differences between G_{zH} and G_{zB} (Fig. 3e) were compared by computing D_{KL} and using resampling analyses to evaluate whether this empirical value could have resulted from D_{KL} values computed from randomly resampled distributions of peak and trough differences in G_{zH} and G_{zB}. The results of this analysis are shown in Fig. 3f, where the distribution of D_{KL} computed from 10^6 randomly resampled distributions is shown as the histogram at left and the empirical D_{KL} value is shown at the arrowhead. This analysis demonstrates that the probability of the empirical D_{KL} value arising from randomly sampled difference measures is less than 10^{-6}, strongly inferring that the empirical D_{KL} could not arise from random resampling of G_{zH} and G_{zB} magnitudes. This supports the conclusion that inflight peak G_{zH} exhibited a greater difference from peak G_{zB} compared to the differences in trough G_{zH} and G_{zB}. This finding demonstrates a consistent asymmetry between the differences between peak G_{zH} and G_{zB}, and trough G_{zH} and G_{zB}, strongly inferring that the factors underlying the differences are dissimilar. This could arise from head stabilization mechanisms leading to greater G_{zH} attenuation during wing downstroke.

Insofar as the analyses of G_{zH} and G_{zB} differences at the maximum peaks and troughs demonstrated asymmetries that inferred a motor paradigm of inflight head stabilization, alternatives to this interpretation were explored through simple models that reconciled static head and body tilt. These alternative models led to evaluations of whether the differences in G_{zH} and G_{zB} could be reproduced by simulations of G_z modulated through wingbeat cycles and superimposing static tilts of head or body. The framework for interpreting relative head and body acceleration magnitudes along G_{zH} and G_{zB} axes is illustrated in Fig. 4, showing simple models of representative conditions in which head and body are coupled (Fig. 4a–c). The relative head and body positions are depicted by the "stick" figures, and the motion tags are represented by the maroon and cyan rectangles affixed to head and body, respectively. In each case shown in Fig. 4, head and body accelerations are coupled throughout each wingbeat cycle. Wingbeat-driven modulations of simulated G_{zH} (sG_{zH}, maroon) and G_{zB} (sG_{zB}, cyan) are modeled as 8 Hz sinewaves (0.125 s period) in the plots of G_z vs. time beneath each figure, with the magnitudes approximating empirical values (Fig. 3a, b). G_{zH} and G_{zB} amplitudes are biased by the head and body tag orientations relative to Earth gravity and the modulation through the wingbeat cycle.

Three conditions in which head and body kinematics are coupled are shown in Fig. 4a–c. The characteristic features of these conditions were the fixed relationships of acceleration magnitudes at peak and trough sG_{zH} and sG_{zB}. Figure 4a shows a representation of the condition in which head and body motion tags were orthogonal to Earth gravity and wingbeat modulation of G_z, resulting in comparable amplitudes of sG_{zH} (solid maroon sine) and sG_{zB} (dashed cyan sine) at both maximum wing downstroke (peak) and wing upstroke (trough). In this condition, sG_{zH} and sG_{zB} were modulated symmetrically around 1*g*.

The condition represented in Fig. 4b is one in which the body tag was orthogonal (i.e., optimally oriented) to Earth gravity and wingbeat-generated acceleration along the G_z axis, but the head was pitched down relative to the

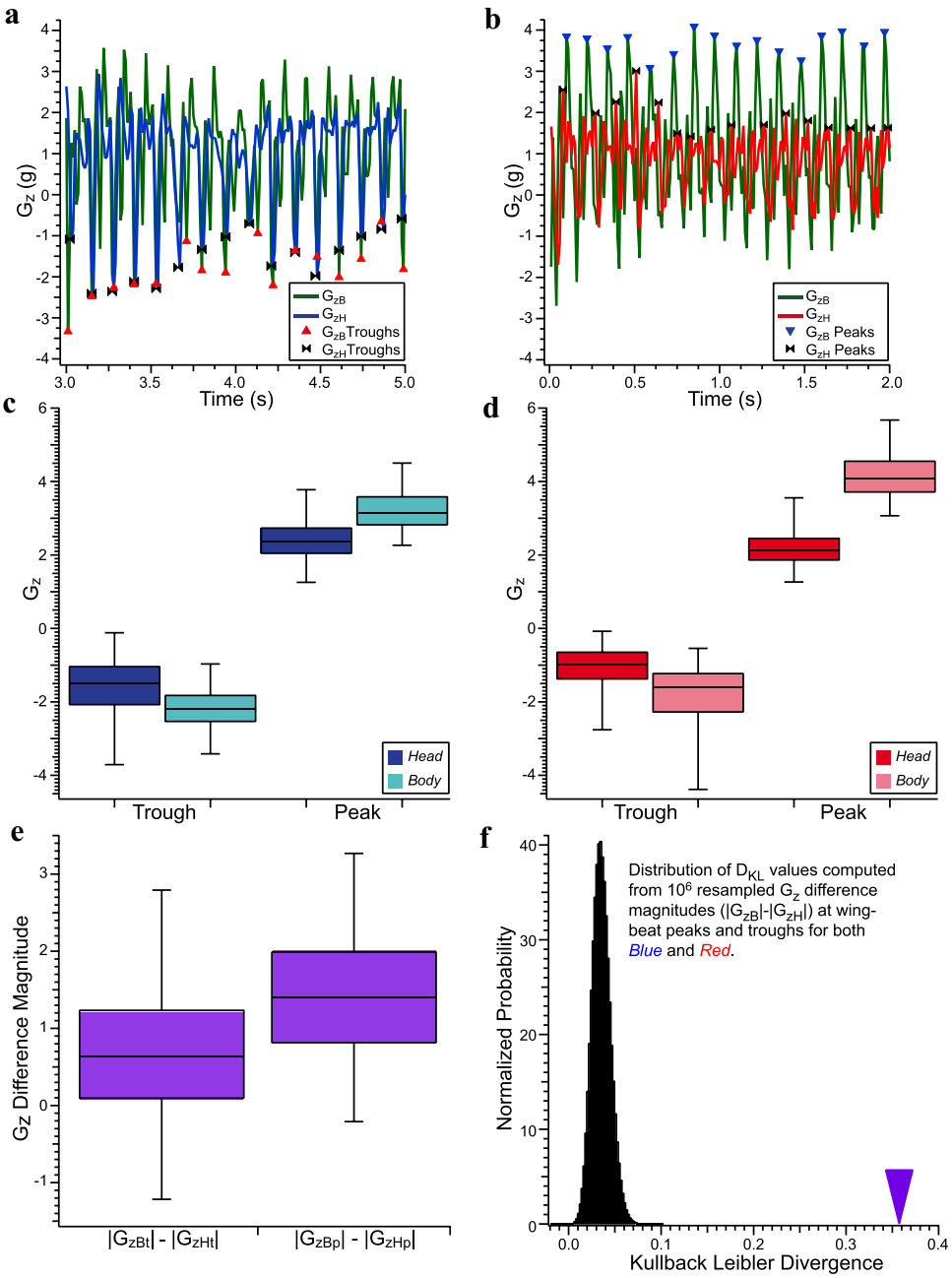

Fig. 3 G_{zH} maxima associated with wing downstroke (peaks) and upstroke (troughs) were attenuated relative to corresponding G_{zB} maxima, and exhibited peak and trough asymmetries. **a**, **b** Representative G_{zH} and G_{zB} for *Blue* (**a**) and *Red* (**b**) *R. aegyptiacus* subjects for two-second flight epochs, illustrating the identification of troughs (see marker legends in **a**) and peaks (see marker legends in **b**). These records illustrate that the differences in G_{zH} and G_{zB} peaks are greater than the differences in G_{zH} and G_{zB} troughs. **c**, **d** The distributions of G_{zH} and G_{zB} peaks and troughs for *Blue* (**c**) and *Red* (**d**) subjects are represented as box-and-whisker plots, further illustrating that the differences between G_{zH} and G_{zB} peaks are greater than the differences between G_{zH} and G_{zB} troughs. **e** For each cycle, the differences in absolute values between trough and peak G_{zB} and G_{zH} measure were obtained, and the distributions of these differences are represented in box-and-whisker plots. **f** The D_{KL} was determined for the empirical distributions (value at inverted triangle), and was compared to D_{KL} values computed from 10^6 resampled distributions (histogram at left). This analysis indicates that the probability of obtaining the empirical D_{KL} from random resampling the trough and peak differences is less than 10^{-6}

body. In this orientation, the head tag was not optimally oriented for Earth-vertical sensing and therefore the acceleration magnitudes were less than those registered by the body tags. This is depicted in the two maroon sinusoids representing 30° (solid sine) and 60° (dashed sine) nose-down pitch. Additionally, however, each wingbeat-generated sG_{zH} waveform was modulated about a reduced static magnitude due to the nose-down head pitch reflecting a static offset proportional to the cosine of the pitch angle (i.e., 0.87 and 0.5 for the 30° and 60° nose-down condition). Since head and body were coupled, the magnitudes in maximum downstroke and upstroke sG_{zH} were similarly attenuated compared to sG_{zB}, and modulated around the static offsets $< 1g$. This attenuation in sG_{zH} would be similar in a nose-up head pitch.

The third example of head and body coupling (Fig. 4c) depicts the condition in which the head was orthogonal and optimally positioned to detect Earth gravity and the wingbeat acceleration vectors in G_z, but the body was pitched (either up or down). As shown for head pitch in Fig. 4b, body pitch angles of 30° and 60° were simulated in Fig. 4c with comparable changes in sG_{zB} magnitudes. In this condition the modulation in sG_{zH} exceeded sG_{zB}, and the relative magnitudes modulated around static offset values were

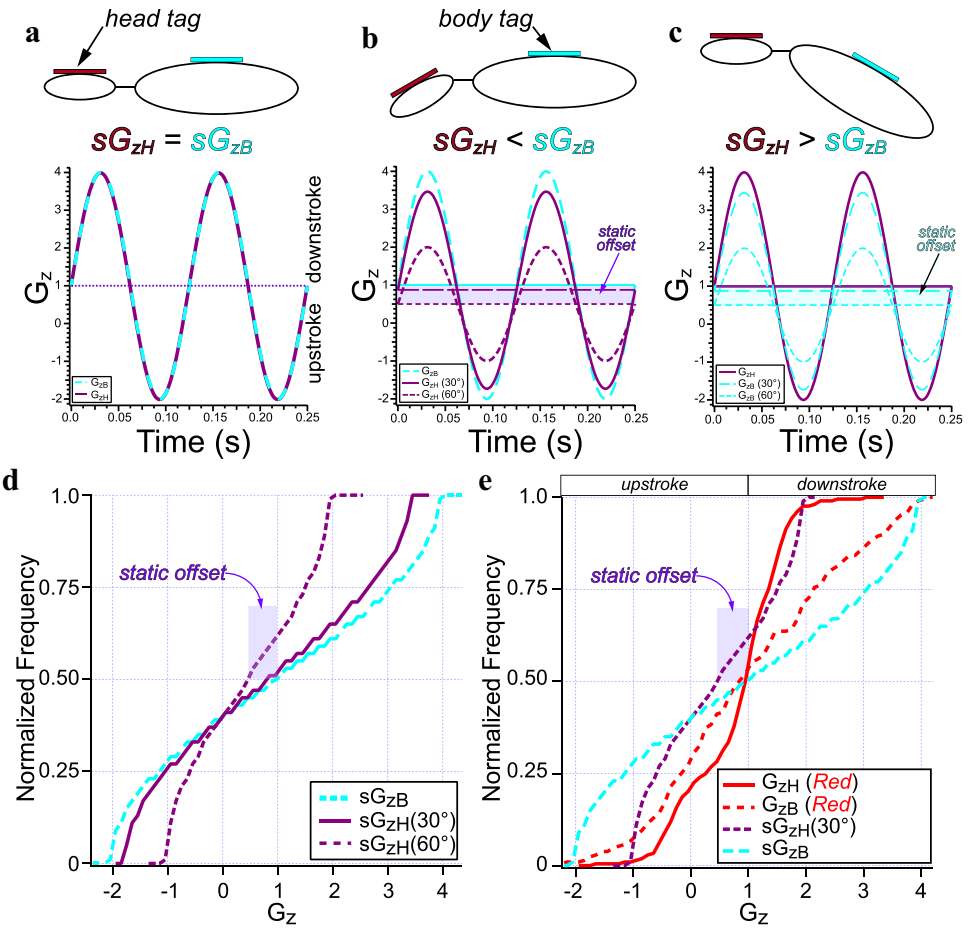

Fig. 4 Model of head and body coupling, in which head tilt mediated static offset in G_{zH} resembles peak and trough G_{zH} asymmetry, is not consistent with empirical distributions of G_{zH}. The coupling of head and body kinematics results in fixed relationships between simulated G_{zH} (sG_{zH}) and G_{zB} (sG_{zB}) that depend upon the orientation of the motion tags relative to Earth-gravity and the wingbeat-associated acceleration vector. *a.* Alignment of head and body tags normal to Earth gravity results in equal modulation of sG_{zH} and sG_{zB}. *b.* The coupling of head and body under conditions of body orthogonal to Earth gravity and static head tilt (e.g., 30°, solid maroon sine, and 60°, dashed maroon sine) results in sG_{zB} modulation around 1*g* and sG_{zH} modulation around static offsets < 1*g* (i.e., proportional to tilt magnitude, illustrated by dashed horizontal line and filled area for 60° tilt). Under these conditions, sG_{zH} is always attenuated relative to sG_{zB}, and the differences between sG_{zH} and sG_{zB} at the peaks and troughs are asymmetric, resembling that shown in Fig. 3. **c** The coupled condition in which the head tag is orthogonal to Earth gravity but the body tag is tilted results in sG_{zB} that is attenuated and offset from 1*g*. This condition was rarely observed in the inflight measures where G_{zH} was greater than G_{zB}. **d**, **e** Normalized cumulative histograms of sG_{zB}, sG_{zH} (30°), and sG_{zH} (60°) illustrate the prominent static offset under the 60° tilt condition. These data are replotted in **e** with a representative flight from the Red subject. Despite the fact that peak and trough sG_{zH} (60°) are similar to peak and trough G_{zH} (Red), the kinematic measures are clearly distinguished by the absence of static offset in G_{zH} (Red). These data illustrate that inflight G_{zH} is not consistent with the sG_{zH} models

similar to those shown in Fig. 4b. For the vast majority of the 986 wingbeat cycles analyzed in the present investigation, peak and trough G_{zB} exceeded G_{zH}, indicating that the condition illustrated in Fig. 4c was only rarely observed and therefore will not be further discussed.

The head and body kinematics simulated in Fig. 4b represented the condition resulting in sG_{zH} modulation that, while attenuated relative to sG_{zB}, was symmetric around a similarly attenuated ambient gravity measurement (i.e., static offset < 1*g*). Despite the fact that the absolute magnitudes of sG_{zH} at maximum downstroke and upstroke were similar, the offset modulation reduced the overall amplitude of sG_{zH} at the peaks and troughs where the mean sG_{zH} under the nose-down pitch conditions was equivalent to the magnitude of the static offset (i.e., 0.87*g* and 0.5*g* for the 30° and 60° pitch conditions, respectively). This gave the *appearance* of asymmetry when comparing G_{zH} and G_{zB} at the peaks and troughs (i.e., magnitude at maximum downstroke and upstroke), mimicking the inflight asymmetry exhibited by G_{zH} and G_{zB} illustrated in Fig. 3. Under these conditions, however, simulated head and body kinematics were coupled and the asymmetry in G_z magnitudes resulted from the static head pitch

giving the appearance of head stabilization when derived from raw G_z measurements alone. Consequently, asymmetry based solely on G_{zH} and G_{zB} magnitude differences at the peaks and troughs may be ambiguous with respect to the interpretation regarding stabilization derived from these measurements. In the case of head and body coupling and the associated symmetric *modulation*, the asymmetry based upon magnitude differences resulted solely from the static offset due to nose-down pitch. Therefore, demonstration that empirical G_{zH} was not associated with a similar static offset would eliminate the possibility that the empirical asymmetry resulted from the conditions similar to those depicted in the simulation (i.e., head–body coupling and static offset).

To further explore the static offset characteristic in modulated head and body kinematics the simulated measures of G_z shown in Fig. 4b were plotted as normalized cumulative distributions in Fig. 4d that include sG_{zB} (cyan, dashed), sG_{zH} (30°) (maroon, solid), and sG_{zH} (60°) (maroon, dashed). These data clearly illustrate the offsets associated with each sG_{zH} measure as those associated with normalized frequencies of 0.5 for each distribution (sinusoidal mean and median). Notably, the offset associated with sG_{zH} (60°) was 0.5, highlighted by the shaded box filling the space between 0.5 and 1g. The simulation corresponding to 30° tilt exhibited a more modest offset (0.87g) and exhibited larger amplitudes at the peaks and troughs (approximately −1.7g and 3.4g).

While the static tilt models of sG_{zH} modulation are distinguished by their offsets from 1g, inflight G_{zH} for both *Blue* and *Red* did not exhibit comparable offset levels. This is exemplified in Fig. 4e, in which the normalized cumulative distributions for sG_{zB} and sG_{zH} (60°) are plotted with inflight G_{zB} (Red) and G_{zH} (Red) for a representative flight of the *Red* subject. These plots demonstrate that the ranges of sG_{zB} and G_{zB} (Red), as well as the ranges for sG_{zH} (60°) and G_{zH} (Red), were very similar. Furthermore, sG_{zB} and G_{zB} (Red) exhibited G_z levels of approximately 1g at the normalized frequency of 0.5. Despite the fact that sG_{zH} (60°) and G_{zH} (Red) exhibited close to the same overall G_z range, G_{zH} (Red) magnitude at the normalized frequency of 0.5 was close to 1g (mean $G_z = 0.82g$ for the entire flight epoch). These data show that G_{zH} (Red) exhibited very small offsets, and therefore the magnitudes at the peaks and troughs were not consistent with a static offset. The magnitude asymmetry is also apparent, where downstroke G_{zH} (Red) measures (i.e., G_{zH} > mean G_{zH}) extended approximately 1.7g (approx. 0.8–2.5g), while upstroke G_{zH} measures extended approximately 2.3g (approx. 0.8 to −1.5g). The range of mean G_{zH} measures for all 50 flights between both subjects was 0.71–1.08g (mean = 0.91g).

The distributions of G_{zH} (Red) from sG_{zH} (60°) were further compared by computing the empirical D_{KL} followed by resampling analyses ($n = 10^6$) to determine the probability that the distribution of G_{zH} (Red) could have been derived by random sampling with sG_{zH} (60°). It was determined that this probability was very low ($p = 0.00299$), further indicating that the underlying factors leading to G_{zH} (Red) were not similar to those producing sG_{zH} (60°).

Estimates of G_{zH} gain confirm kinematic asymmetry and head stabilization

Asymmetries in the magnitudes of peak and trough G_{zH} were further analyzed by computing the distributions of respective G_{zH} gains for the 986 wingbeat cycles for both subjects (Fig. 5a). Overall, G_{zH} gains at the wingbeat peaks were lower than at the troughs, where the distributions exhibited medians of −13.57 dB and −5.63 dB, respectively. These data indicated that G_{zH} was smaller relative to G_{zB} at the peaks compared to the relative G_{zH} magnitude at the troughs. These distributions were compared by computing D_{KL} for the empirical distributions, and then conducting resampling analyses ($n = 10^6$) to determine the probability that the empirical value of D_{KL} could have been derived by chance. The results of this analysis are shown in Fig. 5b, where the histogram reflects 10^6 values of D_{KL} resulting from random resampling of G_{zH} gains from both peak and trough distributions. The empirical D_{KL} value (0.407) was well outside the range of 10^6 resampled D_{KL} values, and therefore the probability that the empirical value could be derived from random resampling was less than 10^{-6}. This analysis confirms that G_{zH} exhibits greater attenuation during wing downstroke and wing upstroke, resulting in the kinematic asymmetry.

Association of tongue click onset with head kinematics suggests relationship of acoustic probing with wingbeat cycle

The analyses of inflight head and body kinematics indicated that the *R. aegyptiacus* subjects exhibited head stabilization behaviors during the downstroke phase of the wingbeat cycle. One interpretation of this behavior is that it limits head movement during echolocation probing of the environment to stabilize inflight sensory gaze (Eitan et al. 2019). If this is true, it might be expected that the preponderance of tongue clicks were emitted during this period of the wingbeat cycle. To evaluate this possibility, recordings from the head tag ultrasonic microphone were analyzed to first identify the tongue click emissions, and then determine the precise time of first emission of the click-doublet. We then determined G_{zH} and G_{zB} at these times as illustrated in Fig. 6a, demonstrating identification of the tongue click onset [yellow diamonds superimposed on the acoustic recording, *Pressure* (Pa; axis at lower right) vs *Time* (s)] and G_{zH} estimated at these times by interpolation. Of the 50 flight epochs evaluated in both subjects (25 each), a total

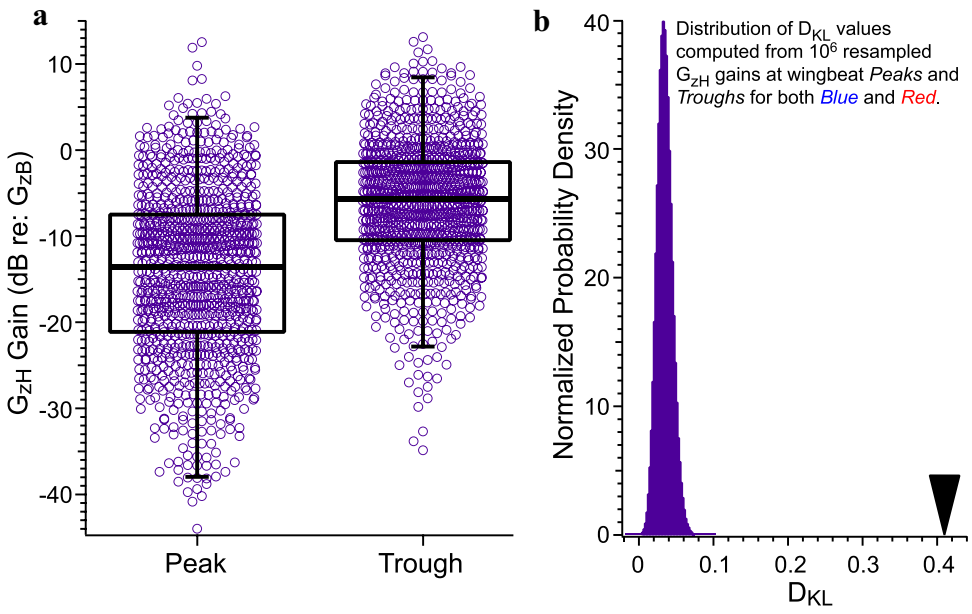

Fig. 5 G_{zH} gains (dB re: G_{zB}) confirm asymmetry in head kinematics at maximum wing downstroke and upstroke. **a** Distributions of G_{zH} gains at peak and trough, corresponding to maximum downstroke and upstroke of 986 wingbeat cycles in both subjects, shown as box-and-whisker plots. The overall lower gains at wingbeat peaks reflect the smaller G_{zH} magnitude relative to the corresponding G_{zB} magnitude. **b** Resampling analyses of D_{KL} illustrate that the probability of computing the empirical D_{KL} value (i.e., 0.407, inverted triangle) from random sampling of peak and trough G_{zH} gains (histogram, $n = 10^6$) is less than 10^{-6}

of 525 click emissions were identified (i.e., *Red*: $n = 197$; *Blue*: $n = 328$). The distributions of G_{zH} at click onset for *both* subjects are shown in Fig. 6b as box-and-whisker plots, illustrating that G_{zH} was $\geq 1g$ at the time of the first click for approximately 75% of the clicks in both subjects. As shown in Figs. 2 and 6, G_{zH} measures $\geq 1g$ correspond to wing downstroke, and therefore these data demonstrate that most (i.e., approximately 75%) of click onset times occurred during wing downstroke. In view of the similarity in this behavior in both subjects, the data were combined to produce a single distribution of first-click G_{zH} measures ($n = 525$), for which the median was found to be $1.41g$.

To further evaluate whether the association between G_{zH} and first-click of a sonar doublet could be associated with head stabilization behavior, we tested the null hypothesis that the median G_{zH} from the combined 525 first-click events could have been derived from random association of click onset times and G_{zH}. The distribution of G_{zH} measures resulting from random resampling is shown in the histogram of Fig. 6c along with the median value from the empirical first-click G_{zH} measures. This analysis demonstrates that the probability of obtaining the empirical median G_{zH} (i.e., $1.41g$) from random associations of G_{zH} and click onset was less than 10^{-6}, supporting rejection of the null hypotheses. Note that the distribution of random G_{zH} medians ranged from 1.0 to 1.3, reflecting the bias of inflight $G_{zH} > 1g$. A comparable resampling analysis was also determined for G_{zB} (not shown), producing a similar result as for G_{zH} wherein the probability of deriving the empirical G_{zB} median from a random association of G_{zB} and click onset was less than 10^{-6} and supporting rejection of the null hypothesis. If the associations between G_{zH} and G_{zB} and click onset were not random, they must be due to underlying factors driving the associations.

Discussion

Echolocation probing during wing downstroke

Previous investigators have interpreted head stabilization behaviors during locomotion as the result of neural mechanisms optimizing sensory gaze (Goldberg and Cullen 2011; Kress et al. 2015; Brooks and Cullen 2019; Dietrich and Wuehr 2019b; Eitan et al. 2019; Dietrich et al. 2020). If similar mechanisms apply to acoustic gaze stabilization during echolocation, it would be expected that inflight emission of sonar signals would be temporally associated with periods of head stabilization. Data from the present study provide strong evidence for head stabilization in *R. aegyptiacus* during wing downstroke where $G_{zH} > 1$ (Figs. 3, 4). Furthermore, the onset of sonar doublets occurred during periods where $G_{zH} > 1$, consistent with the implementation of head stabilization mechanisms to enhance acoustic gaze. Bootstrap resampling analyses showed that the empirical distribution of G_{zH} at sonar click onset was not random (Fig. 6c; $p < 10^{-6}$), supporting the hypothesis that bats stabilize their heads at the time of sonar emissions. These findings are, therefore, consistent with the notion that *R. aegyptiacus* execute behaviors to stabilize acoustic gaze during sustained flight.

The correlation between onset of echolocation emission and wingbeat has been established in many laryngeal echolocating species (Suthers et al. 1972; Jones 1994; Kalko 1994; Wong and Waters 2001; Holderied and von Helversen

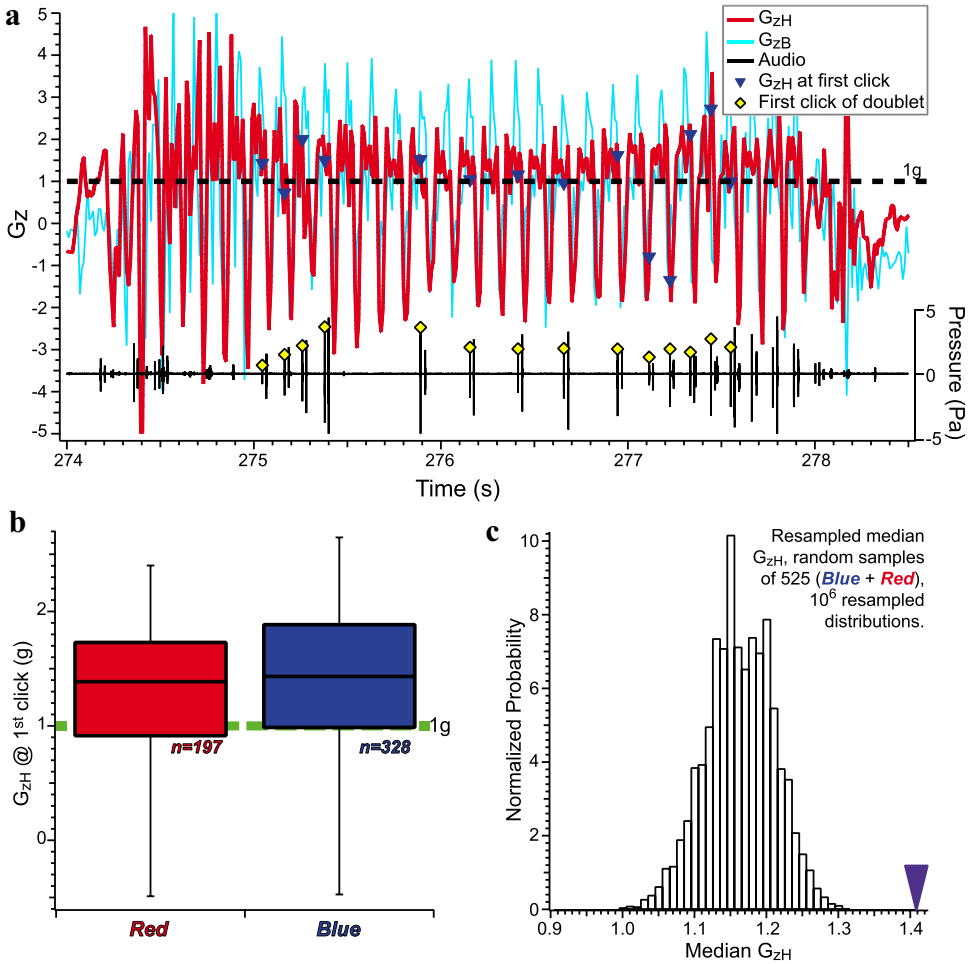

Fig. 6 Onset times of tongue clicks exhibit greater likelihood of occurring at $G_{zH} > 1$ and the period of head stabilization. **a** Representative record of G_{zH}, G_{zB}, and the associated audio recording of representative tongue click doublets. These data illustrate the identification of tongue click onsets shown by the red-filled diamonds superimposed on first click of the doublets. The corresponding values of G_{zH} at these times are identified by the inverted blue triangles. For the 14 identified onset times, 10 corresponded to $G_{zH} > 1g$ (71%). **b** The distributions of G_{zH} at first click onsets for each of the *R. aegyptiacus* subjects are shown as box-and whisker plots, illustrating the similarity in their distributions. **c** The data from both subjects were combined to test the null hypothesis that the median G_{zH} value from all G_{zH} measures corresponding to first click onset times could be derived from random association of onset time with G_{zH}. The histogram represents median G_{zH} resulting from 10^6 resampled distributions of 525 random association between click onset and G_{zH}. The empirical median is shown as the inverted triangle at approx. $1.41g$, indicating the low probability ($p < 10^{-6}$) that the empirical median could be medians computed from 10^6 random distributions

2003; Yartsev and Ulanovsky 2013; Falk et al. 2015). In laryngeal echolocators, emissions were coupled to expiration and wing upstroke, and it was proposed that this may be driven by energy efficiencies (Suthers et al. 1972; Jones 1994; Kalko 1994; Wong and Waters 2001; Holderied and von Helversen 2003). The coupling of wingbeat/respiration and call timing reduces the energetic costs of echolocation (Speakman and Racey 1991), even under flight conditions with high energy demands (Voigt and Lewanzik 2012). A more recent analysis provided evidence that high intensity echolocation calls can impose high metabolic demands (Currie et al. 2020), suggesting that energy efficiencies under these conditions may be derived by coupling sonar calls to expiration and wing upstroke. Yartsev and Ulanovsky (2013) previously showed that echolocation signal production was correlated with wingbeat in the Egyptian fruit bat, *R. aegyptiacus*. However, because lingual echolocation in this species is not driven by respiration, it is unlikely that the coupling of echolocation signal production and wingbeat would offer any energetic advantage as may occur in laryngeal echolocators. This rationale further supports the conclusion that the temporal correlation of sonar signal onset and wingbeat optimizes acoustic gaze stabilization in *R. aegyptiacus*.

Head stabilization may be dependent upon behavioral state

Through the present study direct measurements of G_{zH} demonstrated that sustained flight of *R. aegyptiacus* exhibited wingbeat cycle modulation of at least 3*g* (estimated from the difference in median peak and trough G_{zH}, Fig. 3c, d). At wingbeat frequencies of approximately 8 Hz this G_{zH} range corresponded to peak-to-peak displacements of approximately 8 mm. Eitan et al. (2019) reported that *R. aegyptiacus* exhibited dramatically attenuated inflight vertical gaze angles compared to body-target angles during approach to a landing target. They suggested that this represented head stabilization behaviors serving acoustic gaze optimization during a landing task. The data on vertical gaze angle (determined from continuous tracking of head position relative to the fixed target) did not appear to exhibit similar wingbeat cycle modulation as body-target angle exhibited periods of very little deviation.

Despite the evidence of head stabilization in Egyptian fruit bats, revealed by video recording of head and body kinematics, data from the present investigation of sustained flight in the same species showed robust modulation of head acceleration phase-locked to body acceleration and wingbeat cycle (Figs. 3, 6). Therefore, it appears that head stabilization during the target approach studied by Eitan et al. (2019) may be more refined than those exhibited during periods of sustained flight as shown in the present investigation. A direct comparison of the head displacement magnitudes under the two flight conditions was not feasible in view of the different measurement parameters obtained by Eitan et al. (2019) and the present study. Such a comparison would be invaluable to better understand heterogeneities in behavioral state-dependent acoustic gaze stabilization.

Though the mechanisms of inflight head stabilization in bats have not been directly investigated, mechanical analyses of head movement gain attenuation in whooper swans provided insight into how this may be achieved (Pete et al. 2015). In these animals, head movements exhibited symmetric attenuation relative to body movements, which was modeled as a static gain reduction through the wingbeat cycle that could be achieved by neuromuscular tone-mediated modulation of neck stiffness. Though the morphology of head and body linkage is vastly different in bats compared to whooper swans, a simple extension of the neck stiffness model may explain the asymmetries in *R. aegyptiacus* through differential modulation in phase with wing downstroke and upstroke. Further investigation will be required to test this possibility.

Could inflight kinematics be influenced by loads imposed by head- and body-mounted tags?

The use of miniature body-affixed sensors to measure various attributes of natural behaviors broadly expands the repertoire of documentable characteristics by enabling high resolution measurement capabilities unrestricted by either cabling or the limitations of video documentation. The potential disadvantage is that they impose additional loads to the experimental subjects, which could potentially affect the behaviors under investigation. As previously noted, Stidsholt et al. (2019) found no evidence that adding a single 2.6-g motion tag influenced the flight characteristics of two bat species, *Nyctalus noctule* and *Eptesicus fuscus*, for which the tags added as much as 20% of the animals' body mass. Other investigations that implemented body-mounted tags on larger bats [*Rhinopoma microphyllum*, 40–45 g, carried tags amounting to > 5% body mass (Cvikel et al. 2015); *R. aegyptiacus*, approx. 180 g, carried tags amounting to approximately 12% body mass (Danilovich et al. 2015)] arrived at similar conclusions. Egert-Berg et al. (2018) tagged five species with devices (microphone and GPS) representing up to 15% additional loads as well as lighter tags, and concluded that additional loading represented no deleterious effects on flight and foraging behavior. These data suggest that inflight behaviors of species investigated in the aforementioned studies were very robust to additional loads.

Despite the stability in general flight characteristics to modest passive loads, the potential impact of the 2.6-g head motion tag upon head kinematics measurements was further scrutinized. Although the present dataset was not sufficient to unequivocally exclude the possibility that the attenuation in peak G_{zH} during wing downstroke was influenced by load imposed by the motion tag, multiple lines of evidence suggested that any effect of passive head loading would be small. Non-instrumented *R. aegyptiacus* subjects exhibited robust head stabilization behaviors during target identification and landing tasks in the dark and without any head load (Eitan et al. 2019). The findings of the present study under loaded conditions and sustained flight were consistent with this result, and suggest that head stabilization is an integral component of natural acoustic gaze stabilization in *R. aegyptiacus* and not compromised by head- and body-mounted instrumentation. Furthermore, estimates of head mass in *R. aegyptiacus* (obtained from cadaver specimens) indicated that it represented approximately 12% of total body mass, suggesting that head masses of the two subjects of the present study were 19 and 26 g (*Blue* and *Red*, respectively). The 2.6-g motion tags, then, imposed relative loads of 13% and 10% of head mass in these subjects, respectively. It might be expected that, if the head tag imposed a performance-challenging load to diminish G_{zH} gain relative to G_{zB},

a concomitant effect on G_{zH} phase would also have been observed, appearing as a consistent timing delay. Despite these loads, head acceleration remained tightly synchronized with body acceleration (i.e., time at maximum upstroke; see Fig. 3a, b), providing no indication of a phase shift consistent with effects associated with the head load. Therefore, while an impact of the modest head and body loading on flight performance cannot be entirely excluded, the data available from the present investigation suggest that the loads did not impact the basic findings reported here.

Vestibular contribution to acoustic gaze stabilization

The neural mechanisms supporting sensory gaze stabilization during locomotion are not completely understood. As described for visually dominant species, head stabilization mechanisms likely involve multisystem compensatory reflex circuits that include vestibular reflexes and efference copy from locomotor pattern generators (Straka and Chagnaud 2017; Straka et al. 2018; Brooks and Cullen 2019; Dietrich et al. 2020). Previous investigations provided compelling evidence that efference copy (i.e., "copies" of spinal locomotor pattern generator activity projecting rostrally to CNS circuits serving sensorimotor integration) plays an important role in visual gaze stabilization in late stage larval *Xenopus* (Lambert et al. 2012; Chagnaud et al. 2015). These circuits not only drive compensatory oculomotor behavior in the principal plane of locomotor-associated head movements (Lambert et al. 2012), but also were found to suppress sensory input representing locomotion-associated head movements from the peripheral vestibular epithelia (Chagnaud et al. 2015). The precise mapping of active movement suppression of peripheral vestibular input, however, may not generalize phylogenetically, as comparable suppression of afferent vestibular signaling during active movement was not found in primates (Brooks and Cullen 2014). Dietrich and Wuehr (2019a) recently reported data to potentially reconcile these differences, finding that during human ambulatory activity horizontal gaze remained dependent upon vestibular input while vertical gaze stabilization relied more on efference copy. The latter investigation supports the idea that gaze stabilization is "spatially tuned" to principal locomotor-associated head movements requiring stabilization.

Aerial locomotion in *R. aegyptiacus* appears to be similar to terrestrial locomotion exhibited by bi- and quadrupeds in that both are associated with robust head movements in the Earth-vertical plane (i.e., G_z) (Dietrich and Wuehr 2019a; L.F. Hoffman, unpublished data). Hence, it might be expected that a principal driver of head stabilization in *R. aegyptiacus* is efference copy of wingbeat spinal pattern generators. This would be consistent with the notion posited by Eitan et al. (2019) that enhanced stabilization behavior exhibited by *R. aegyptiacus* was not driven by compensatory vestibular mechanisms. However, vestibular information was shown to contribute to inflight obstacle navigation in echolocating bats (Horowitz et al. 2004). Furthermore, preliminary studies of the peripheral vestibular epithelia in *R. aegyptiacus* revealed cellular adaptations consistent with enhanced high-frequency coding capabilities by semicircular canal cristae compared to terrestrial rodents (L.F. Hoffman, unpublished data). Further investigation of the challenges in sensory integration during high-performance locomotor activity exhibited by bats in flight will advance our general understanding of the neural mechanisms underlying sensorimotor integration and acoustic gaze stabilization.

Supplementary Information The online version contains supplementary material available at https://doi.org/10.1007/s00359-021-01518-x.

Acknowledgements The authors gratefully acknowledge Mark Johnson for development of the motion tags that made this investigation possible.

Author contributions Conceptualization and design of this study was achieved by AS, LS, PTM, CM, and LH. Material preparation and data collection were conducted by AS and LS. Data analyses were completed by JR and LH. The first draft of the manuscript was written by LH, and all authors contributed to the final version. All authors read and approved the final manuscript.

Funding The authors gratefully acknowledge funding support from the National Science Foundation (NCS-FO 1734744 (2017–2021 to CFM), the Air Force Office of Scientific Research (FA9550-14-1-0398NIFTI to CFM), the Office of Naval Research (N00014-17-1-2736 to CFM), Human Frontiers Science Program Fellowship (LT000220/2018 to AS), The Carlsberg Foundation (Semper Ardens grant to PM and LS), and the National Institute on Deafness and Other Communication Disorders (1R21 DC017285 to LH).

Data availability The data will be made available upon request to the corresponding author.

Code availability Custom scripts (Matlab) will be made available upon request to the corresponding author.

Declarations

Conflict of interest All authors declare no competing interests.

Ethics approval All experimental procedures involving animals were conducted at Johns Hopkins University (JHU) and conformed to the protocol approved by the JHU institutional animal care and use committee.

References

Aldridge HDJN (1987) Body accelerations during the wingbeat in six bat species: the function of the upstroke in thrust generation. J Exp Biol 130:275–293

Aldridge H, Brigham RM (1988) Load carrying and maneuverability in an insectivorous bat: a test of the 5% "rule" of radio-telemetry. J Mamm 69:379–382

Brooks JX, Cullen KE (2014) Early vestibular processing does not discriminate active from passive self-motion if there is a discrepancy between predicted and actual proprioceptive feedback. J Neurophysiol 111:2465–2478. https://doi.org/10.1152/jn.00600.2013

Brooks JX, Cullen KE (2019) Predictive sensing: the role of motor signals in sensory processing. Biol Psychiatry Cogn Neurosci Neuroimaging 4:842–850. https://doi.org/10.1016/j.bpsc.2019.06.003

Chagnaud BP, Banchi R, Simmers J, Straka H (2015) Spinal corollary discharge modulates motion sensing during vertebrate locomotion. Nat Commun 6:7982. https://doi.org/10.1038/ncomms8982

Chiu C, Reddy PV, Xian W, Krishnaprasad PS, Moss CF (2010) Effects of competitive prey capture on flight behavior and sonar beam pattern in paired big brown bats, *Eptesicus fuscus*. J Exp Biol 213:3348–3356. https://doi.org/10.1242/jeb.044818

Currie SE, Boonman A, Troxell S, Yovel Y, Voigt CC (2020) Echolocation at high intensity imposes metabolic costs on flying bats. Nat Ecol Evol 4:1174–1177. https://doi.org/10.1038/s41559-020-1249-8

Cvikel N, Egert Berg K, Levin E, Hurme E, Borissov I, Boonman A, Amichai E, Yovel Y (2015) Bats aggregate to improve prey search but might be impaired when their density becomes too high. Curr Biol 25:206–211. https://doi.org/10.1016/j.cub.2014.11.010

Danilovich S, Krishnan A, Lee WJ, Borrisov I, Eitan O, Kosa G, Moss CF, Yovel Y (2015) Bats regulate biosonar based on the availability of visual information. Curr Biol 25:R1124–R1125. https://doi.org/10.1016/j.cub.2015.11.003

Dietrich H, Wuehr M (2019a) Selective suppression of the vestibulo-ocular reflex during human locomotion. J Neurol 266:101–107. https://doi.org/10.1007/s00415-019-09352-7

Dietrich H, Wuehr M (2019b) Strategies for gaze stabilization critically depend on locomotor speed. Neuroscience 408:418–429. https://doi.org/10.1016/j.neuroscience.2019.01.025

Dietrich H, Heidger F, Schniepp R, MacNeilage PR, Glasauer S, Wuehr M (2020) Head motion predictability explains activity-dependent suppression of vestibular balance control. Sci Rep 10:668. https://doi.org/10.1038/s41598-019-57400-z

du Lac S, Raymond JL, Sejnowski TJ, Lisberger SG (1995) Learning and memory in the vestibulo-ocular reflex. Annu Rev Neurosci 18:409–441. https://doi.org/10.1146/annurev.ne.18.030195.002205

Egert-Berg K, Hurme ER, Greif S, Goldstein A, Harten L, Herrera ML, Flores-Martinez JJ, Valdes AT, Johnston DS, Eitan O, Borissov I, Shipley JR, Medellin RA, Wilkinson GS, Goerlitz HR, Yovel Y (2018) Resource ephemerality drives social foraging in bats. Curr Biol 28:3667-3673 e3665. https://doi.org/10.1016/j.cub.2018.09.064

Eitan O, Kosa G, Yovel Y (2019) Sensory gaze stabilization in echolocating bats. Proc Biol Sci 286:20191496. https://doi.org/10.1098/rspb.2019.1496

Falk B, Kasnadi J, Moss CF (2015) Tight coordination of aerial flight maneuvers and sonar call production in insectivorous bats. J Exp Biol 218:3678–3688. https://doi.org/10.1242/jeb.122283

Ghose K, Moss CF (2003) The sonar beam pattern of a flying bat as it tracks tethered insects. J Acoust Soc Am 114:1120–1131

Ghose K, Moss CF (2006) Steering by hearing: a bat's acoustic gaze is linked to its flight motor output by a delayed, adaptive linear law. J Neurosci 26:1704–1710. https://doi.org/10.1523/JNEUROSCI.4315-05.2006

Goldberg JM, Cullen KE (2011) Vestibular control of the head: possible functions of the vestibulocollic reflex. Exp Brain Res 210:331–345. https://doi.org/10.1007/s00221-011-2611-5

Griffin DR, Novick A, Kornfield M (1958) The sensitivity of echolocation in the fruit bat, *Rousettus*. Biol Bull 115:107–113. https://doi.org/10.2307/1539097

Hedenstrom A, Johansson LC (2015) Bat flight: aerodynamics, kinematics and flight morphology. J Exp Biol 218:653–663. https://doi.org/10.1242/jeb.031203

Hedrick TL (2008) Software techniques for two- and three-dimensional kinematic measurements of biological and biomimetic systems. Bioinspir Biomim 3:034001. https://doi.org/10.1088/1748-3182/3/3/034001

Holderied MW, von Helversen O (2003) Echolocation range and wingbeat period match in aerial-hawking bats. Proc Biol Sci 270:2293–2299

Horowitz SS, Cheney CA, Simmons JA (2004) Interaction of vestibular, echolocation, and visual modalities guiding flight by the big brown bat, *Eptesicus fuscus*. J Vestib Res 14:17–32

Jones G (1994) Scaling of wingbeat and echolocation pulse emission rates in bats: why are aerial insectivorous bats so small? Funct Ecol 8:450–457. https://doi.org/10.2307/2390068

Kalko E (1994) Coupling of sound emission and wingbeat in naturally foraging European pipistrelle bats (Microchiroptera: Vespertilionidae). Folia Zool 43:363–376

Kress D, van Bokhorst E, Lentink D (2015) How lovebirds maneuver rapidly using super-fast head saccades and image feature stabilization. PLoS One 10:e0129287. https://doi.org/10.1371/journal.pone.0129287

Lambert FM, Combes D, Simmers J, Straka H (2012) Gaze stabilization by efference copy signaling without sensory feedback during vertebrate locomotion. Curr Biol 22:1649–1658. https://doi.org/10.1016/j.cub.2012.07.019S0960-9822(12)00810-X

Land MF (2015) Eye movements of vertebrates and their relation to eye form and function. J Comp Physiol A 201:195–214. https://doi.org/10.1007/s00359-014-0964-5

Lee WJ, Falk B, Chiu C, Krishnan A, Arbour JH, Moss CF (2017) Tongue-driven sonar beam steering by a lingual-echolocating fruit bat. PLoS Biol 15:e2003148. https://doi.org/10.1371/journal.pbio.2003148

Mackay DJC (2003) Information theory, inference, and learning algorithms. Cambridge University Press, Cambridge

Pete AE, Kress D, Dimitrov MA, Lentink D (2015) The role of passive avian head stabilization in flapping flight. J R Soc Interface 12:0508. https://doi.org/10.1098/rsif.2015.0508

Shanidze N, Kim AH, Loewenstein S, Raphael Y, King WM (2010) Eye-head coordination in the guinea pig II. Responses to self-generated (voluntary) head movements. Exp Brain Res 205:445–454. https://doi.org/10.1007/s00221-010-2375-3

Speakman JR, Racey PA (1991) No cost of echolocation for bats in flight. Nature 350:421–423. https://doi.org/10.1038/350421a0

Stidsholt L, Johnson M, Beedholm K, Jakobsen L, Kugler K, Brinkløv S, Salles A, Moss CF, Madsen PT (2019) A 2.6-g sound and movement tag for studying the acoustic scene and kinematics of echolocating bats. Meth Ecol Evol 10:48–58. https://doi.org/10.1111/2041-210x.13108

Straka H, Chagnaud BP (2017) Moving or being moved: that makes a difference. J Neurol 264:28–33. https://doi.org/10.1007/s00415-017-8437-8

Straka H, Dieringer N (2004) Basic organization principles of the VOR: lessons from frogs. Prog Neurobiol 73:259–309. https://doi.org/10.1016/j.pneurobio.2004.05.003

Straka H, Simmers J, Chagnaud BP (2018) A new perspective on predictive motor signaling. Curr Biol 28:R232–R243. https://doi.org/10.1016/j.cub.2018.01.033

Surlykke A, Ghose K, Moss CF (2009) Acoustic scanning of natural scenes by echolocation in the big brown bat, *Eptesicus fuscus*. J Exp Biol 212:1011–1020. https://doi.org/10.1242/jeb.024620

Suthers RA, Thomas SP, Suthers BJ (1972) Respiration, wing-beat and ultrasonic pulse emission in an echo-locating bat. J Exp Biol 56:37–48

Voigt CC, Lewanzik D (2012) 'No cost of echolocation for flying bats' revisited. J Comp Physiol B 182:831–840. https://doi.org/10.1007/s00360-012-0663-x

Warnecke M, Macias S, Falk B, Moss CF (2018) Echo interval and not echo intensity drives bat flight behavior in structured corridors. J Exp Biol. https://doi.org/10.1242/jeb.191155

Wong JG, Waters DA (2001) The synchronisation of signal emission with wingbeat during the approach phase in soprano pipistrelles (*Pipistrellus pygmaeus*). J Exp Biol 204:575–583

Yartsev MM, Ulanovsky N (2013) Representation of three-dimensional space in the hippocampus of flying bats. Science 340:367–372. https://doi.org/10.1126/science.1235338

Yovel Y, Falk B, Moss CF, Ulanovsky N (2010) Optimal localization by pointing off axis. Science 327:701–704. https://doi.org/10.1126/science.1183310

Yovel Y, Falk B, Moss CF, Ulanovsky N (2011) Active control of acoustic field-of-view in a biosonar system. PLoS Biol 9:e1001150. https://doi.org/10.1371/journal.pbio.1001150